Reversible Tuning of Magnetization in a Ferromagnetic Ruddlesden–Popper-Type Manganite by Electrochemical Fluoride-Ion Intercalation

*Sami Vasala, Anna Jakob, Kerstin Wissel, Aamir Iqbal Waidha, Lambert Alff, and Oliver Clemens**

Electrical tuning of materials' magnetic properties is of great technological interest, and in particular reversible on/off switching of ferromagnetism can enable various new applications. Reversible magnetization tuning in the ferromagnetic Ruddlesden–Popper manganite $La_{2-2x}Sr_{1+2x}Mn_2O_7$ by electrochemical fluoride-ion (de)intercalation in an all-solid-state system is demonstrated for the first time. A 67% change in relative magnetization is observed with a low operating potential of <1 V, negligible capacity fading, and high Coulombic efficiency. This system offers a high magnetoelectric voltage coefficient, indicating high energy efficiency. This method can also be extended to tune other materials' properties in various perovskite-related materials.

1. Introduction

Magnetoelectric control, that is, using an electric field to control material's magnetic properties (magnetic state, moment, ordering temperature, etc.) is of great fundamental interest, but also enables various applications, such as spin-based electronics, magnetic data storage, micromagnetic actuation, and sensors.[1,2] Depending on the application, there can be different requirements on the magnetoelectric system, such as high magnetic on/off ratio, long-term

Dr. S. Vasala, A. Jakob, K. Wissel, A. I. Waidha, Prof. O. Clemens
Technische Universität Darmstadt
Institut für Materialwissenschaft
Fachgebiet Materialdesign durch Synthese
Alarich-Weiss-Straße 2, 64287 Darmstadt, Germany
E-mail: oliver.clemens@md.tu-darmstadt.de
Prof. L. Alff
Technische Universität Darmstadt
Institut für Materialwissenschaft
Fachgebiet Dünne Schichten
Alarich-Weiss-Straße 2, 64287 Darmstadt, Germany
Prof. O. Clemens
Karlsruhe Institute of Technology
Institute for Nanotechnology
Hermann-von-Helmholtz-Platz 1, 76344 Eggenstein-Leopoldshafen
Germany

The ORCID identification number(s) for the author(s) of this article can be found under https://doi.org/10.1002/aelm.201900974.

stability and reversibility, speed of operation, or a particular operating voltage range or temperature. While various magnetoelectric systems already exist,[1,2] new approaches to control magnetic material properties are still sought after in order to improve on the different requirements for different applications. There, a special focus lies in materials which possess a high magnetoelectric voltage coefficient $\alpha = \Delta M/(\Delta V \times M)$ (the change of relative magnetization, $\Delta M/M$, per applied voltage, ΔV), as it provides for high energy efficiency in applications.[1,2]

Many systems used for electrochemical tuning of magnetism rely on the application of field-induced strain[3–8] or charge-carrier doping via gate dielectrics.[9–14] While these methods offer the possibility of fast operation, they tend to have low magnetoelectric coefficients and be volatile.[1,2] Electrically driven, reversible ion exchange within an electrochemical cell is a promising method to modify materials' magnetic properties. Essentially, the target material is placed as an electrode in a battery cell and can be charged (ions inserted into or removed from the structure) or discharged (ions removed from or inserted into the structure), leading to changes in oxidation states and structural properties (bond distances/angles or lattice strain), which in turn affect the material's magnetic properties. Such an approach can offer large changes in magnetic properties (as material's full volume can be accessed), high electrical efficiency (as there is no need for continuous power to maintain a charged/discharged state), and non-volatility (as the material's properties remain unchanged when the power is off).

This approach has been demonstrated with various Li-ion battery chemistries,[15–19] with the highest changes in magnetization (≈90%) found for the Fe to Fe_2O_3 conversion reaction.[15] Nearly complete on/off switching has also been found for other electrochemical conversion reactions, for example in the Fe-FeOx[20] and Co-CoOx[21] systems or in nanoporous Pd(Co).[22] However, such conversion-based systems may suffer from long-term stability and reversibility issues due to complicated reaction mechanisms, which can lead to side reactions and formation of unwanted phase. To overcome these issues, intercalation of ions into a suitable host lattice appears to be a more promising method, as it can cause less drastic chemical and structural changes. Using various spinel-type iron oxides as electrodes, 10–70% changes in magnetization have been achieved by Li-ion intercalation.[16–18]

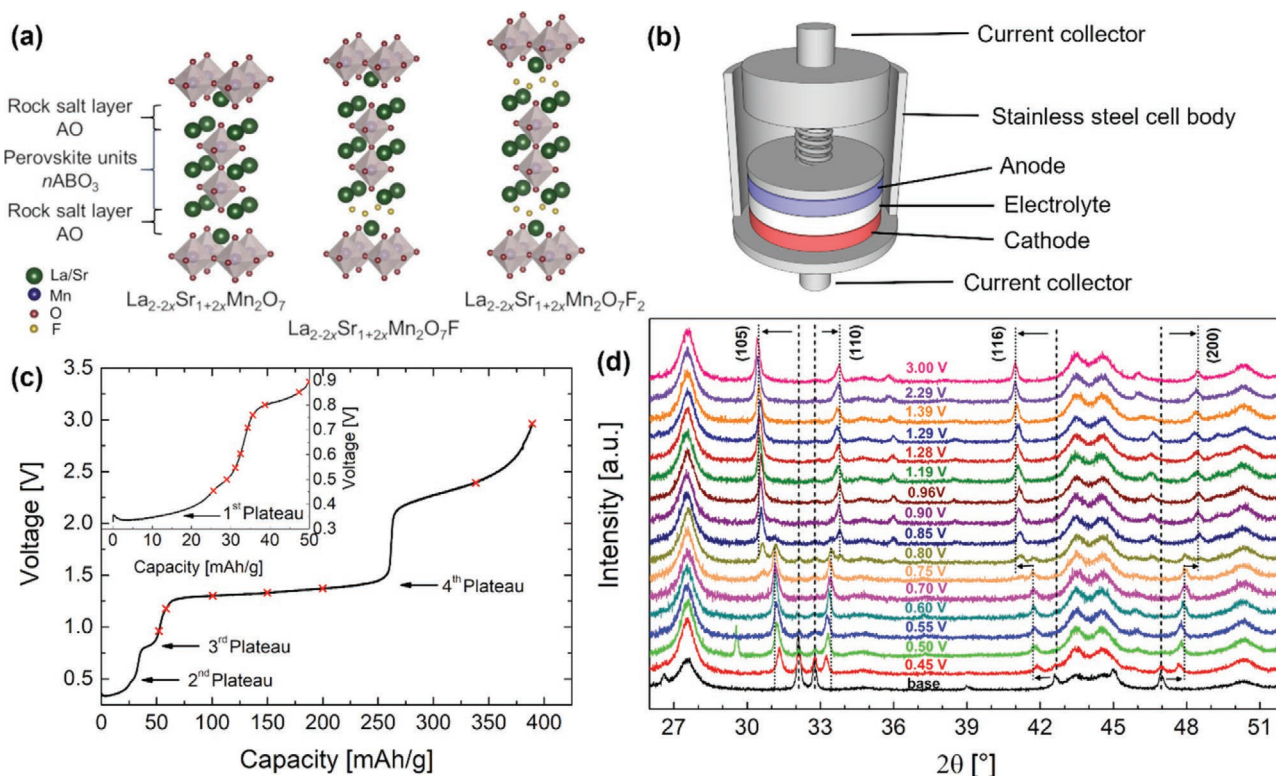**Figure 1.** a) The ideal $n = 2$ RP-type structures of $La_{2-2x}Sr_{1+2x}Mn_2O_7$ and the corresponding fluorinated phases $La_{2-2x}Sr_{1+2x}Mn_2O_7F_1$ and $La_{2-2x}Sr_{1+2x}Mn_2O_7F_2$ with either one or two rock salt layers filled, respectively. b) Schematic of the Swagelok-type cell used in the electrochemical measurements. c) Typical charging curve for a $La_{1.3}Sr_{1.7}Mn_2O_7/La_{0.9}Ba_{0.1}F_{2.9}/Pb\text{-}PbF_2$ cell. The inset shows details of the lower capacity range and the red crosses mark the chosen cut-off voltages for the charging process. d) Ex situ diffraction patterns obtained for the individual cells charged to different cut-off voltages. The most indicative reflections for the lattice parameter change of the RP-type phase during fluorination are marked. The additional reflection at $\approx 29.5°$ is caused by a silicon sample holder. Broad reflection groups (e.g., at 27.5, 43.5, 44.5, and 50.5°) correspond to the solid electrolyte phase $La_{0.9}Ba_{0.1}F_{2.9}$. A full refinement of a single pattern with partial fit curves for the different phases is exemplarily shown in the Supporting Information.

Apart from lithium ions, also fluoride ions can be intercalated into or deintercalated from suitable host structures within so-called fluoride-ion batteries.[23–25] Compared to the Li-ion, fluoride enables the use of materials that are only accessible with anion intercalation and deintercalation, most notable of which are the various perovskite-related structures,[26–30] such as the $A_{n+1}B_nO_{3n+1}$ Ruddlesden–Popper (RP) system. This RP structure can be understood as being built up of n perovskite blocks interleaved by rock salt layers which can host an additional anion such as fluoride (**Figure 1**a). As for perovskites, RP-type materials are known for their wide range of magnetic properties and offer therefore a promising host-lattice for novel magnetoelectric applications within a so-far unexplored system.

Here we demonstrate for the first time the use of fluoride-ion intercalation as a method to reversibly tune material's magnetic properties. We selected the $n = 2$ RP phase $La_{2-2x}Sr_{1+2x}Mn_2O_7$ as our target material for magnetic tuning. This compound has two rock salt layers per unit cell; experiments using chemical fluorination have shown that these layers can be fluorinated in separate steps, forming either $La_{2-2x}Sr_{1+2x}Mn_2O_7F_{1-x}$ or $La_{2-2x}Sr_{1+2x}Mn_2O_7F_{2-x}$,[31,32] as presented in Figure 1a. The magnetic states of $La_{2-2x}Sr_{1+2x}Mn_2O_7$ range from double-exchange mediated ferromagnetism (FM) to antiferromagnetism and are highly sensitive to the Mn oxidation state and distance between the perovskite building blocks,[33] making it

an optimal material for tuning of magnetic properties. In this work, the composition $La_{1.3}Sr_{1.7}Mn_2O_7$ was selected, as it is FM with a high magnetic moment of >3 μ_B Mn^{-1} and has the highest Curie temperature ($T_C \approx 120$ K) within this system.[33] We show that a 67% reversible change in magnetization is possible in this material by fluoride ion (de)intercalation, comparable to the best Li-ion intercalation systems. What is more, our operating potentials of <1 V are lower than those typically required for the Li-ion intercalation (≈ 2 V),[1,2] leading to higher magnetoelectric efficiency α.

2. Results and Discussion

2.1. Impact of Charging/Fluorination on the Structural and Magnetic Properties

Details on the as-synthesized $La_{1.3}Sr_{1.7}Mn_2O_7$ and the prepared cathode composite are presented in Figures S1–S4, Tables S1 and S2, Supporting Information. In short, the $La_{1.3}Sr_{1.7}Mn_2O_7$ was found to be single phase and the diffraction patterns could be refined using the $I4/mmm$ RP $n = 2$ aristotype structure.[34] Titration results confirmed an oxidation state of Mn of +3.35, as expected for a composition of $La_{1.3}Sr_{1.7}Mn_2O_7$. Long-range FM ordering was found with a $T_C \approx 117$ K and $M(H)$ measurements

at 10 K showed a saturation magnetization of ≈ 3.6 μ_B Mn^{-1} corresponding well with the expected value ($0.65 \cdot 4$ μ_B + $0.35 \cdot 3$ μ_B = 3.65 μ_B). To ensure that $La_{1.3}Sr_{1.7}Mn_2O_7$ was not modified within the cathode composite by preparation or heating during charging, the structural parameters and magnetic properties of the parent oxide, the as-prepared cathode composite and a heated cathode composite were compared. These samples did not differ significantly from each other, showing that $La_{1.3}Sr_{1.7}Mn_2O_7$ is stable in the cell environment.

All the electrochemical measurements were done on solid-state $La_{1.3}Sr_{1.7}Mn_2O_7/La_{0.9}Ba_{0.1}F_{2.9}/Pb\text{-}PbF_2$ cells, loaded in a modified Swagelok-type cell body, a schematic of which is shown in Figure 1b. Figure 1c shows a typical charging curve of such a cell up to 3 V. Three short plateaus occur below a specific charge capacity of 60 mAh g^{-1}: one at the very beginning at ≈ 0.34 V and two others at ≈ 0.45 V and ≈ 0.8 V, respectively. In addition, a long plateau at ≈ 1.3 V can be observed. In order to understand the structural changes during the charging process, separate cells were charged to different cut-off voltages ($V_{C, charge}$) and ex situ XRD measurements were performed on the cathode side of the cells (the chosen cut-off voltages are marked in Figure 1c and the charging curves of the individual cells are presented in Figure S5, Supporting Information). Diffraction patterns measured for the cells with different cut-off voltages are shown in Figure 1d and Rietveld refinement

results can be found in Figure S6 and Table S3, Supporting Information. At low voltages, $La_{1.3}Sr_{1.7}Mn_2O_7F_{1-x}$ is formed at the cost of the initial $La_{1.3}Sr_{1.7}Mn_2O_7$ phase. Starting at ≈ 0.75 V, $La_{1.3}Sr_{1.7}Mn_2O_7F_{1-x}$ is transformed into the higher fluorine content phase $La_{1.3}Sr_{1.7}Mn_2O_7F_{2-x}$. No indication is given for the formation of further phases at higher potentials. Thus, the first two charging plateaus (at ≈ 0.34 and ≈ 0.45 V) can be assigned to redox reactions leading to a single-layer intercalation of fluorine and the third plateau (at ≈ 0.8 V) corresponds to the insertion of fluorine into the second interstitial layer. It is noteworthy that the capacity for the higher voltages exceeds the theoretical capacity for a storage of two fluoride ions (≈ 98 mAh g^{-1}) by far. This agrees well with earlier findings of Nowroozi et al.,[27,29,35] which suggest that the long plateau at ≈ 1.3 V is related to the fluorination of carbon black.

The relative weight fractions (RWFs) and lattice parameters of the three phases present in the charged cells are plotted as a function of $V_{C, charge}$ in **Figure 2**a–c. Evidently, the single-layer intercalation of fluoride reaches its maximum at 0.7 V (RWF of $La_{1.3}Sr_{1.7}Mn_2O_7F_{1-x}$ is 100%), whereas the second layer is completely filled at around 0.9 V (RWF of $La_{1.3}Sr_{1.7}Mn_2O7F_{2-x}$ reaches 100%). For $V_{C, charge} \leq 0.7$ V, the presence of two phases (the initial $La_{1.3}Sr_{1.7}Mn_2O_7$ and the single-layer fluorinated phase) is observed. Thus, instead of forming a single phase with an average fluoride content and an intermediate oxidation
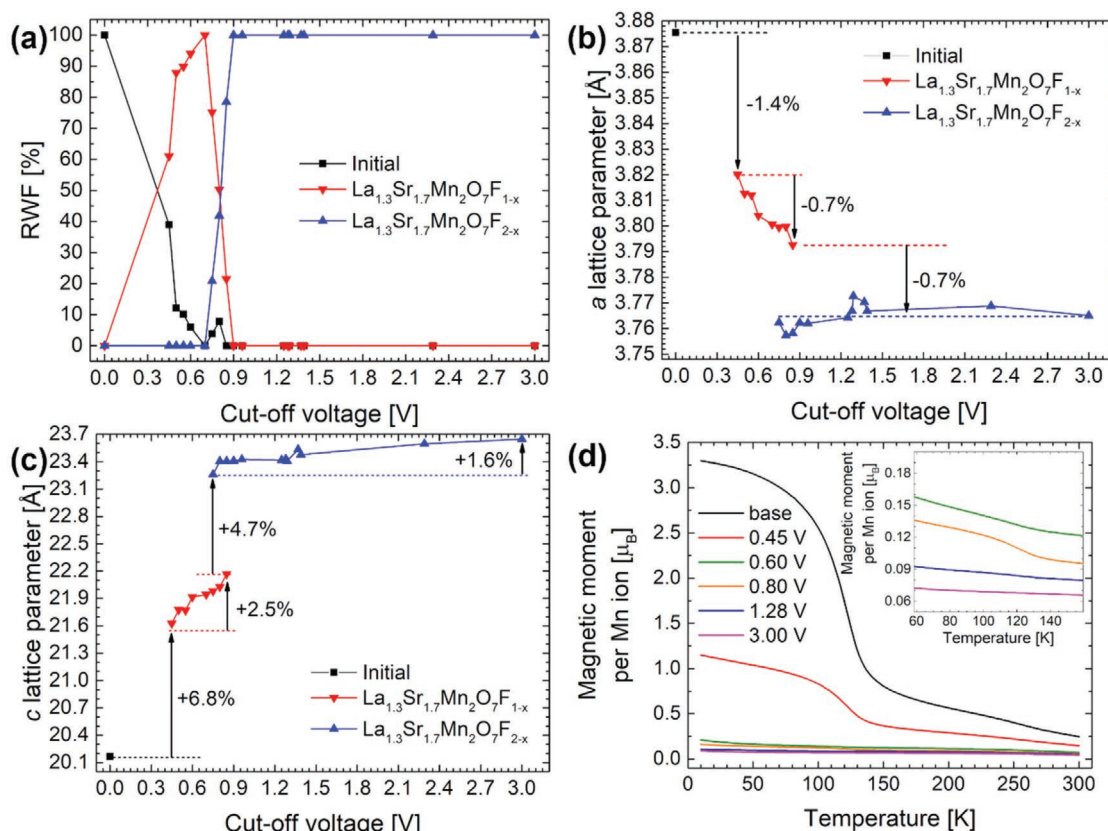

Figure 2. a) RWFs for the phases formed on charging to the selected cut-off voltages. b), c) Trends of the a and c lattice parameters for the different phases as a function of the charging cut-off voltage. Lines only serve as guides for the eye. d) $M(T)$ curves for the cathode composites of cells charged to different cut-off voltages (FC mode, 1 T field). The inset shows the temperature region in which a small FM transition occurs for the cells charged to 0.6 and 0.8 V. The sample denoted as "base" represents the cell which was heated 10 days at 170 °C without charging.

**ADVANCED
SCIENCE NEWS**
www.advancedsciencenews.com

**ADVANCED
ELECTRONIC
MATERIALS**
www.advelectronicmat.de

state of the Mn ions, the system seems to prefer to exist in a fluorinated phase with an increased oxidation state and a non-fluorinated phase with a lower oxidation state. Based on the specific charge capacities for cells with cut-off voltages ≤ 0.7 V and the RWFs of the different phases, an estimation of the average fluoride content of the fluorinated $La_{1.3}Sr_{1.7}Mn_2O_7F_{1-x}$ phase could be made (see Table S4, Supporting Information). It appears that fluoride contents smaller than ≈0.6 per formula unit are unstable, so that a mixture of a higher fluorinated phase ($La_{1.3}Sr_{1.7}Mn_2O_7F_{1-x}$ with $x < 0.4$) and the non-fluorinated initial phase is formed. For a cut-off voltage of 0.7 V, the average fluoride content is around 0.65 and $La_{1.3}Sr_{1.7}Mn_2O_7F_{1-x}$ is stable as a single phase without (or with only traces) of the initial phase. Around 0.8 V the fluorination of the second rock salt layer starts and the initial phase reappears. The RWF of the initial phase increases to almost 8%, while being ≈ 0% at 0.7 and 0.9 V. This suggests that also for the $La_{1.3}Sr_{1.7}Mn_2O_7F_{2-x}$ phase, there is a certain stability range for the fluoride content below which the system prefers to form a mixture of the non-fluorinated initial phase and a higher fluorinated $La_{1.3}Sr_{1.7}Mn_2O_7F_{2-x}$ phase, instead of a single phase with an average fluoride content. However, we emphasize that the quantification of the stability range of the $La_{1.3}Sr_{1.7}Mn_2O_7F_{2-x}$ phase is hindered by the presence of two fluorinated phases with unknown fluoride contents. This phase separation could be caused either by redox disproportion (a phase of intermediate oxidation state converts to two different phases, one of higher and one of lower oxidation state) or by structural changes that make phases with an average fluoride content energetically unfavorable.

The lattice parameters in Figure 2b,c show that the fluorination of $La_{1.3}Sr_{1.7}Mn_2O_7$ leads to a reduction of the lattice parameter a (due to oxidation of Mn and a subsequent decrease in ionic radius), while parameter c was increased. The c parameter increased by ≈9.4% by the single-layer intercalation of fluorine and then by another ≈6.3% on further charging to 3 V due to the intercalation of fluorine into the second rock salt layer ($La_{1.3}Sr_{1.7}Mn_2O_7$ ($c ≈ 20.17$ Å) → $La_{1.3}Sr_{1.7}Mn_2O_7F_{1-x}$ ($c ≈ 22.17$ Å) → $La_{1.3}Sr_{1.7}Mn_2O_7F_{2-x}$ ($c ≈ 23.65$ Å), see Table S3, Supporting Information, for details). The changes in lattice parameters are in good agreement with those reported for the chemical fluorination of $La_{1.2}Sr_{1.8}Mn_2O_7$ ($c ≈ 20.14$ Å) to $La_{1.2}Sr_{1.8}Mn_2O_7F$ ($c ≈ 21.72$ Å) and $La_{1.2}Sr_{1.8}Mn_2O_7F_2$ ($c ≈ 23.38$ Å).[31,32]

Figure 2d presents $M(T)$ curves of cathode composites of selected cells charged to different cut-off voltages. The data show that the electrochemical fluorination of $La_{1.3}Sr_{1.7}Mn_2O_7$ leads to a significant change in magnetic properties; even charging to a cut-off voltage of 0.45 V reduced the magnetic moment at 10 K in a 1 T field by more than a half. For all cut-off voltages above 0.45 V, at 10 K only a very weak magnetic moment exists (≤0.2 μ_B). Furthermore, there is a clear correlation between the phase composition and magnetic properties. Charging a cell up to 0.45 V reduces the RWF of the initial $La_{1.3}Sr_{1.7}Mn_2O_7$ phase from 100% to ≈39%. Comparing the values of the magnetic moment/Mn at 10 K in 1 T field, an equivalent decrease to ≈37% is observed. Similarly, the cells charged to 0.6 and 0.8 V only showed a very weak FM transition, while the cells charged to 1.28 and 3 V did not exhibit such a feature at all. This corresponds well with the observation

of a RWF of the initial $La_{1.3}Sr_{1.7}Mn_2O_7$ phase of 6 and 7.8% for the former cells, respectively, while the latter did not show traces of the initial phase. It is therefore clear that the fluorinated phases do not show FM properties and any FM interactions observed in the charged cells are caused by residual fractions of the initial phase. Due to the fact that the charging leads to a mixture of the initial FM $La_{1.3}Sr_{1.7}Mn_2O_7$ phase and a non-FM $La_{1.3}Sr_{1.7}Mn_2O_7F_{1-x}$ phase at low cut-off voltages, the observed T_C remains practically unchanged by the fluorination even though the overall magnetization decreases.

2.2. Impact of Discharging/Defluorination on the Structural and Magnetic Properties

For reversible magnetization tuning, a suitable cut-off voltage for the charging process must be high enough to show a significant change in the magnetic properties (in the ideal case a complete on-off magnetic switching). Furthermore, the voltage should be as low as possible to allow for high efficiency, shortest possible charging times and lowest possible volume changes, and to avoid oxidative side reactions of carbon black (at ≈1.3 V), which might lead to reduced cyclability of the cell. Based on these criteria, charging cut-off voltages of 0.45 and 0.6 V were chosen. **Figure 3**a,b presents typical charge–discharge curves for cells charged to 0.45 or 0.6 V and discharged to −3 V. For the $V_{C, charge} = 0.45$ V cells, the discharge curve shows a clear plateau at ≈0.1 V, whereas for the $V_{C, charge} = 0.6$ V cells an additional small plateau appears at ≈0.2 V, corresponding to the small secondary plateau in the charging curve. Below these voltages several other less well-defined plateaus are also seen. To investigate the structural changes during discharging, separate cells were charged to 0.45 or 0.6 V and then discharged to selected voltages $V_{C, discharge}$ (see Figure 3a,b, with the charge–discharge curves of the individual cells presented in Figures S7 and S8, Supporting Information). Diffraction patterns for these cells are shown in Figure 3c,d and the Rietveld refinement results can be found in Figure S9, Tables S5 and S6, Supporting Information. For both charging voltages, the discharged cells show a decrease in the fluorinated phase and an increase in the initial $La_{1.3}Sr_{1.7}Mn_2O_7$ phase. However, compared to the charged-only cells, the discharged cells reveal the presence of an additional phase. This phase is referred to here as a "residual fluoride phase." The detailed nature of this new phase is currently not known, but a trapping of residual fluoride ions in the interlayer site would be a plausible explanation for the formation of the new phase, as its lattice parameters ($a ≈ 3.87$ Å, $c ≈ 20.51$ Å) are between those of the initial $La_{1.3}Sr_{1.7}Mn_2O_7$ phase and the $La_{1.3}Sr_{1.7}Mn_2O_7F_{1-x}$ phase (see Supporting Information for details and also the discussion of magnetic properties later in the text).

Figure 3e,f shows the RWFs of the three phases present in the discharged cells. Evidently, the discharging greatly reduces the RWF of the $La_{1.3}Sr_{1.7}Mn_2O_7F_{1-x}$ phase, with a notable increase in the RWF of the residual fluoride phase. The RWF of the initial $La_{1.3}Sr_{1.7}Mn_2O_7$ phase also increases, although to a lower extent. For both initial charging conditions, the RWF of the $La_{1.3}Sr_{1.7}Mn_2O_7$ phase reaches its maximum at a discharge cut-off voltage of about −0.3 V (≈54% for $V_{C, charge} = 0.45$ V and
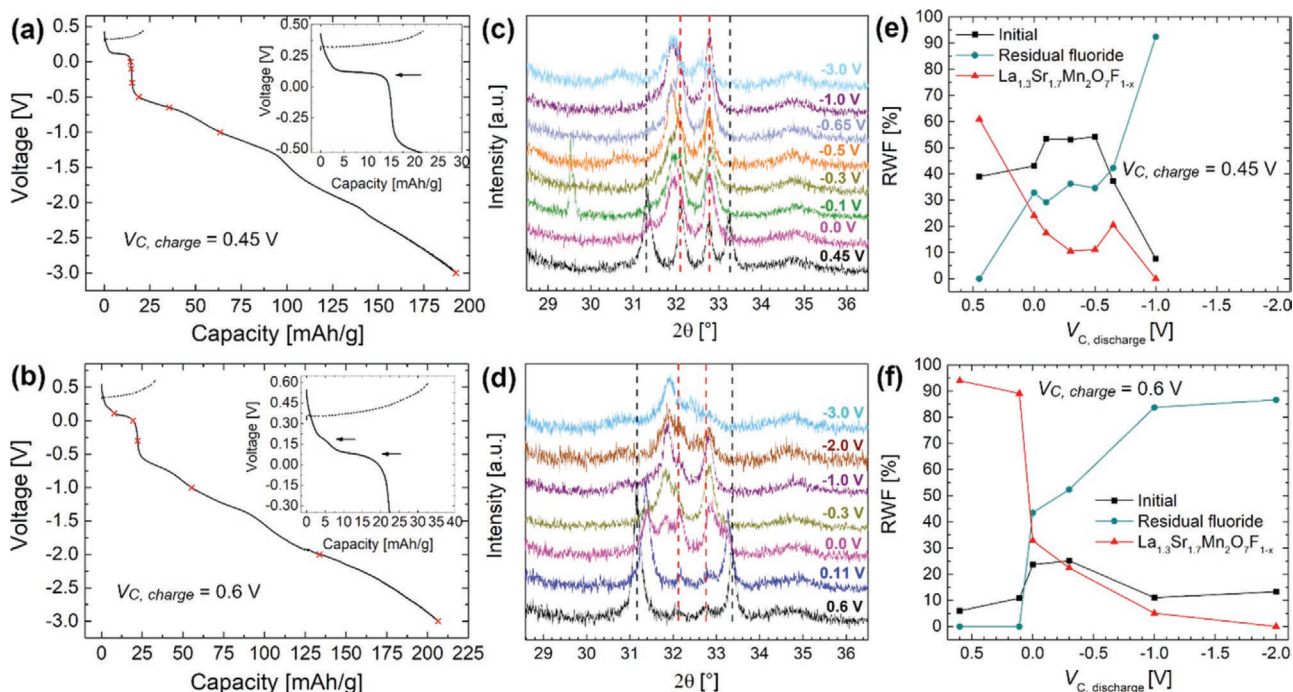
Figure 3. Typical charge–discharge curves for cells charged to a) $V_{C, charge}$ = 0.45 or b) 0.6 V. The insets show details of the lower capacity ranges and the red crosses mark the chosen cut-off voltages for the discharging process. Representative diffraction patterns for the individual cells charged to c) $V_{C, charge}$ = 0.45 or d) 0.6 V, and discharged to different cut-off voltages. The red and black dotted lines indicate the reflection positions of the initial $La_{1.3}Sr_{1.7}Mn_2O_7$ phase and the $La_{1.3}Sr_{1.7}Mn_2O_7F_{1-x}$ phase, respectively. RWFs of the phases observed for cells charged to e) $V_{C, charge}$ = 0.45 or f) 0.6 V on discharging to different cut-off voltages. Lines only serve as guide for the eye.

≈25% for $V_{C, charge}$ = 0.6 V, respectively). Discharging below −0.3 V decreases the RWF of the $La_{1.3}Sr_{1.7}Mn_2O_7F_{1-x}$ phase, but at the same time the residual fluoride phase appears to be stabilized instead of the initial phase. Thus, it is evident that defluorination is possible to a certain extent, but the maximum obtainable RWF of the initial phase is limited. The discharging cut-off voltage $V_{C, discharge}$ = −0.3 V seems to provide a good compromise in order to maximize the RWF of the $La_{1.3}Sr_{1.7}Mn_2O_7$ phase and was thus selected for cell cycling tests.

Figure 4a shows $M(T)$ curves for cells charged to 0.45 or 0.6 V and discharged to −0.3 V, together with the charged-only cells. As is evident, the FM interactions can be partially restored by

the discharging. For $V_{C, charge}$ = 0.45 and 0.6 V, about 57% and 20% of the initial $La_{1.3}Sr_{1.7}Mn_2O_7$ magnetic moment at 10 K in 1 T field was restored on discharging to −0.3 V, respectively. These values correspond well to the RWFs of $La_{1.3}Sr_{1.7}Mn_2O_7$ in these cells, showing that the FM properties are dominantly caused by the $La_{1.3}Sr_{1.7}Mn_2O_7$ phase and that the residual fluoride phase is not ferromagnetic. This indicates that also small amounts of fluoride ions within the rock salt interlayers can be sufficient to distort the ferromagnetic coupling between the perovskite building blocks by increasing their distance to each other. For the cells charged to 0.45 V, a Curie temperature of ≈120 K was found for both the charged and discharged cells,
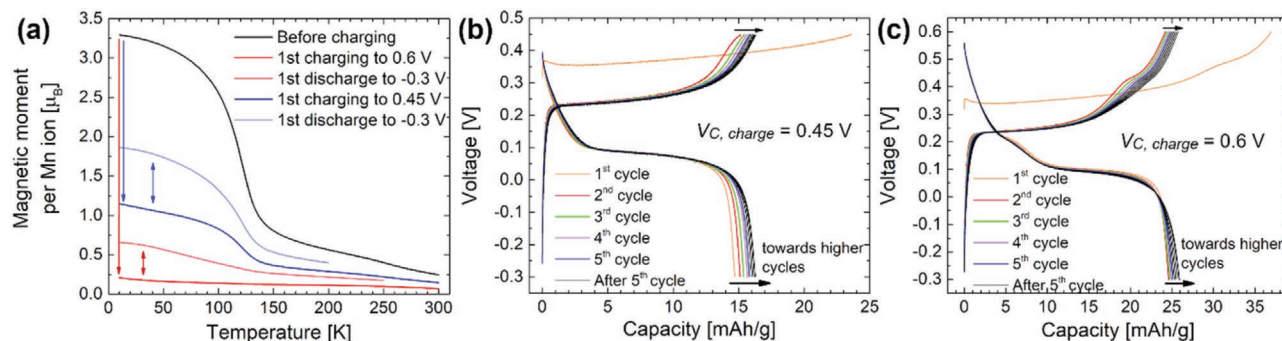
Figure 4. a) $M(T)$ curves (FC mode, 1 T field) for an uncharged $La_{1.3}Sr_{1.7}Mn_2O_7$ cathode composite, cathode composites charged to $V_{C, charge}$ = 0.45 V or 0.6 V and cathode composites charged and discharged to $V_{C, discharge}$ = −0.3 V. The arrows indicate the magnetic changes that occur on charging/discharging. Capacity–voltage curves for cells operated for 10 charge–discharge cycles, with charging cut-off voltages of b) $V_{C, charge}$ = 0.45 V or c) 0.6 V. The first five cycles are colored and the black arrows indicate how the charge/discharge curves behave with increasing cycle number.

**ADVANCED
SCIENCE NEWS**
www.advancedsciencenews.com

**ADVANCED
ELECTRONIC
MATERIALS**
www.advelectronicmat.de

indicating that the recovered $La_{1.3}Sr_{1.7}Mn_2O_7$ phase is only slightly modified during the charging cycle. In contrast, the cell charged to 0.6 V and discharged to −0.3 V showed a different behavior; the transition temperature range was notably widened and the Curie temperature was lowered to ≈60 K. This change could be due to a slight chemical and/or structural inhomogeneity, caused by fluoride ions trapped in the structure due to the deeper charging, which could lead to a wide distribution of FM transition temperatures.

2.3. Reversible Switching of Magnetization Using Optimized Operation Conditions

To verify the reversibility of the magnetization tuning, cells with the cut-off voltage combinations $V_{C, charge}$ = 0.45 or 0.6 V and $V_{C, discharge}$ = −0.3 V were operated for ten charge–discharge cycles. In the following, half-integer cycle numbers refer to cells stopped at charged states and integer cycle numbers refer to cells stopped at discharged states. The charge and discharge curves for these cells are shown in Figure 4b,c. After the first cycle, the plateaus for the charging process shifted to lower potentials by about 0.12 V and the specific charge capacity reduced by about 35%. It appears that during the initial charging step side reactions take place, which facilitate fluorination and defluorination in the subsequent cycles. It is possible that, similar to LIBs, these reactions occur at the interfaces within the cathode material (between the active material and the electrolyte) and lead to a stabilization of electron and fluoride transport through the interfaces. Apparently, interfacial reactions are known to have a decisive effect on battery performance, as they can significantly influence ion and electron conductivity.[36]

After the initial charging step, the cells' behavior remained highly stable for the tested ten cycles. As can be seen from Figure 4b,c, the consecutive charge–discharge curves shift to slightly higher capacities. Thus, there was no capacity fading when the cells were cycled. Instead, the fluoride intercalation seems to slightly increase with the number of cycles. The capacity increase per cycle did not exceed ≈0.35 mAh g^{-1} (in most cases ≈0.2 mAh g^{-1}) and decreased with increasing charge cycles, so that at ten cycles the total cumulative capacity increase was less than 2 mAh g^{-1}. For all cells investigated in this work, the Coulombic efficiency of the first cycle was around 65–75%, while from the second cycle onward, a Coulombic efficiency of 101(2)% was reached. A Coulombic efficiency slightly above 100% could be explained by a reactivation of $La_{1.3}Sr_{1.7}Mn_2O_7F_{1-x}$ formed during the first charging cycle. In addition to the 10 times cycled cells, a single cell was cycled between 0.45 and −0.3 V for 45 cycles (see details in Figure S10, Supporting Information). During this cycling, the features of the charge–discharge curves became slightly more rounded with the increasing number of cycles, but no significant capacity fading or loss of Coulombic efficiency was found. In the context of the desired magnetization tuning, these observations are promising, as a high Coulombic efficiency and a lack of capacity fading are prerequisites for cyclable and stable magnetization changes.

In order to investigate the structural and magnetic changes during the cell cycling, separate cells with the cut-off voltage combinations $V_{C, charge}$ = 0.45 or 0.6 V and $V_{C, discharge}$ = −0.3 V were operated between one and ten cycles, stopping at either the charged or uncharged states, and ex situ XRD and magnetic measurements were done on the cathode composites (see Figure S11–S13, Tables S7 and S8, Supporting Information, for the details). **Figure 5** shows the RWFs of the phases present in the cycled cells. Regardless of the number of cycles, all charged cells contained residues of the initial phase and a large fraction of the $La_{1.3}Sr_{1.7}Mn_2O_7F_{1-x}$ phase, while all discharged cells had a mixture of the initial, residual fluoride and $La_{1.3}Sr_{1.7}Mn_2O_7F_{1-x}$ phases. The phase compositions of the different cells appear relatively consistent after the first charging step, with minor cell-specific variations. The average RWF of the $La_{1.3}Sr_{1.7}Mn_2O_7F_{1-x}$ phase differed by about 73% between the charged and uncharged states for both $V_{C, charge}$ = 0.45 and 0.6 V, indicating that high amounts of the active material contribute to the redox reactions during charging/discharging. On the other hand, between the charging and discharging, the average RWF of the initial FM phase changed between ≈10% and ≈50% for the $V_{C, charge}$ = 0.45 V cells, and between ≈5% and ≈34% for the $V_{C, charge}$ = 0.6 V cells, respectively.

Magnetic data for the cycled cells are presented in Figures S12 and S13, Supporting Information. As before, the Curie temperatures for all the $V_{C, charge}$ = 0.45 V cells were close to the T_C of the as prepared cathode composite (≈120 K), whereas the $V_{C, charge}$ = 0.6 V cells showed broadened transitions with significantly reduced average T_C of 55–68 K. **Figure 6** presents the magnetic moments measured for the cells at 10 K in a 1 T field as a function of the number of cycles. Additionally, the voltage vs. time curves of the cells with ten cycles are shown in order to demonstrate at which points of the charge/discharge process the individual cells were stopped. As is apparent from Figure 6, after the first charging cycle (during which the system is about to stabilize), the change in the magnetization remains constant and well reproducible with respect to increasing number of cycles. The variations between the cells are most likely explained by errors introduced on weighing the small amounts of sample for the subsequent calculation of the magnetic moments. In case of the $V_{C, charge}$ = 0.45 V cells, the charged cells' magnetic moments stabilized to 0.40(7) μ_B Mn^{-1} after the first cycle, while the discharged cells had values of 1.2(2) μ_B Mn^{-1}, with an average magnetic moment change of about 0.84 μ_B Mn^{-1}. For the $V_{C, charge}$ = 0.6 V cells, the charged cells showed moments of 0.22(2) μ_B Mn^{-1}, while for the discharged cells the moments were 0.64(2) μ_B Mn^{-1}, and the moment change was reduced to about 0.42 μ_B Mn^{-1}. Thus, the magnetic moments in case of the $V_{C, charge}$ = 0.45 V cells were approximately twice as high as the cells with $V_{C, charge}$ = 0.6 V, for both the charged and discharged cells, respectively. For both cases, however, this resulted in the same relative magnetization change of 67% between the charged and discharged states. This shows that by choosing a low cut-off voltage in the charging process, the absolute magnetic moments could be increased, but the relative change in magnetization due to the fluoride (de)intercalation remained the same. Due to the fact that the cells can be operated at very low potentials (ΔV = 0.75 or 0.9 V for $V_{C, charge}$ = 0.45 or 0.6 V, respectively), the cells shown here possess among the highest magnetoelectric couplings for tunable magnetic systems observed so far.[1,2] Further, it is interesting to
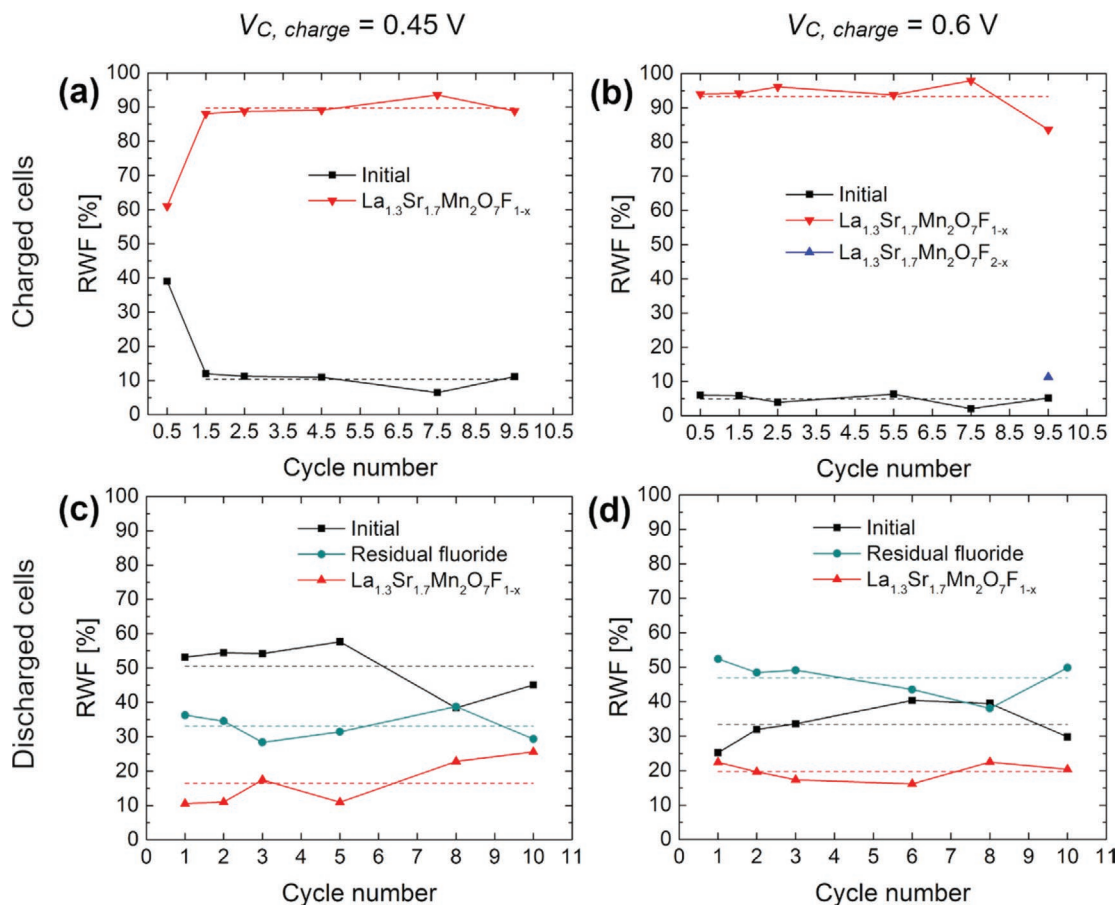
**ADVANCED
SCIENCE NEWS**

www.advancedsciencenews.com

**ADVANCED
ELECTRONIC
MATERIALS**

www.advelectronicmat.de

Figure 5. RWFs of the phases present in cells operated for different numbers of charge–discharge cycles and stopped in a charged state, with a) $V_{C, charge}$ = 0.45 or b) 0.6 V. RWFs of the phases present in cells operated for different number of charge–discharge cycles and stopped in a discharged state, with c) $V_{C, charge}$ = 0.45 or d) 0.6 V. The dotted lines represent the average of the respective RWFs. Lines only serve as guide for the eye.

note that the electrochemically treated samples possess slightly higher coercivities than the $La_{1.3}Sr_{1.7}Mn_2O_7$ base sample, though the coercivity remains stable within errors comparing the different charged and uncharged samples, and appears to be independent on the cut-off conditions (Figure S13, Supporting Information).

3. Conclusions

In conclusion, we have demonstrated for the first time the use of reversible fluoride-ion intercalation for reversible tuning of material's magnetic properties. The selected RP n = 2 compound $La_{1.3}Sr_{1.7}Mn_2O_7$ was cycled between strong and weak FM states, with a 67% maximum change in magnetization, negligible capacity fading and high Coulombic efficiency. This is comparable to the best results obtained by Li-ion intercalation in iron-based spinels, with an additional benefit of one of the highest magnoelectric couplings observed so far due to the use of low cell potentials of <1 V. The maximum change in magnetization is currently limited by the formation of the residual fluoride phase during cell discharging. An increase of the change of magnetization would be possible if the RWF of the initial FM phase could be both reduced in the charged state

and increased in the discharged state. Better understanding of the nature and formation of the unknown residual fluoride phase could help eliminating it in the discharging process. Our work demonstrates the effectiveness of the electrochemical fluoride intercalation for tuning materials' properties; in the future, we will apply this approach to further materials, aiming to bring the magnetic ordering temperature closer to ambient conditions, and to tackle other material properties such as reversible tuning of superconductivity.[37] Additonally, it might be possible to improve the reversibly switchable magnetic moment further, for example, by reducing particle sizes to allow for a more complete extraction of fluoride ions in order to reobtain the defluorinated starting state, or to improve the cycling conditions within the limits explored within this study. Further, the development of higher conducting electrolytes[38,39] for fluoride ion batteries and their combination with RP-type systems might help to improve other important aspects, for example, the dynamics of the system.

4. Experimental Section

Stoichiometric amounts of La_2O_3 (99.9%, Alfa Aesar, predried at 1100 °C before use), $SrCO_3$ (≥98%, Sigma-Aldrich), and Mn_2O_3
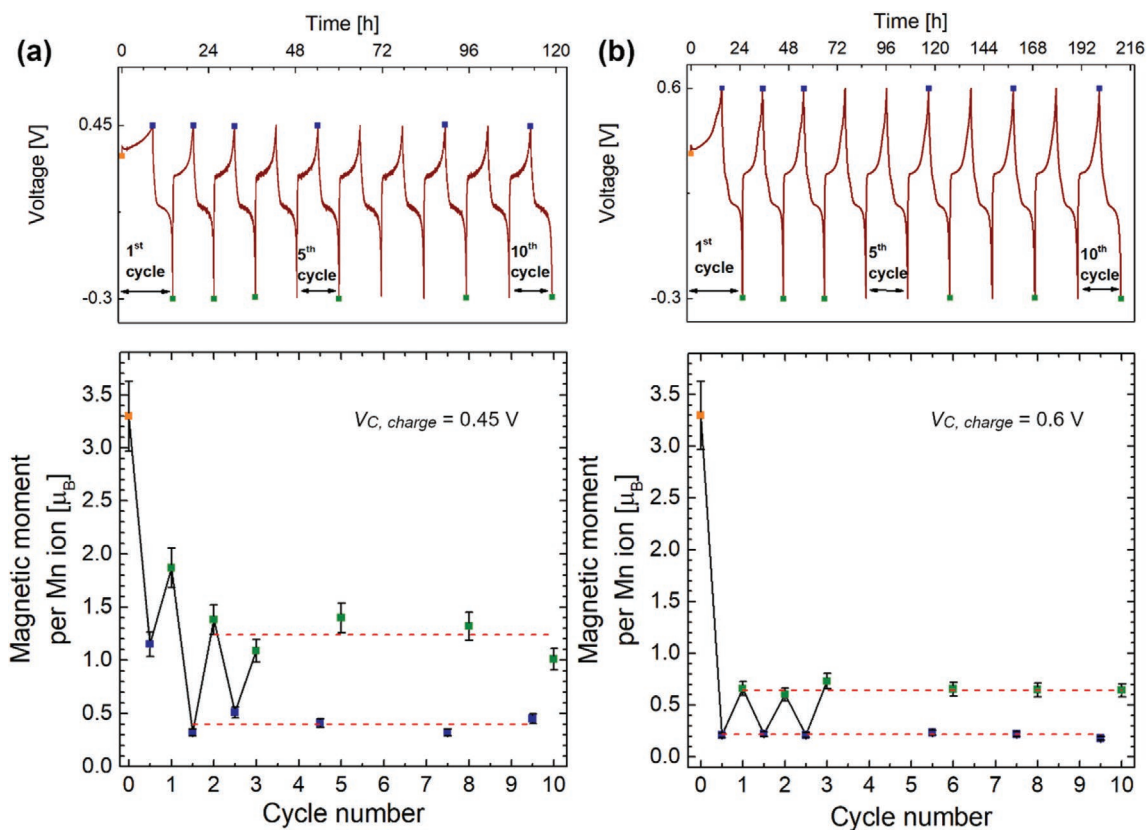
Figure 6. Magnetic moments (10 K, 1 T field) for $La_{1.3}Sr_{1.7}Mn_2O_7$ cathode composites operated for different number of charge–discharge cycles, with a) $V_{C,\,charge} = 0.45$ or b) 0.6 V. Blue/green markers indicate charged/discharged cells, respectively. The top figures show representative voltage–time curves for the cells, indicating where each cell was stopped in the cycling process. The dashed red lines show the average value of the magnetic moments for the charged and discharged states (whereby in case of $V_{C,\,charge} = 0.45$ V, the first cycle is ignored). Lines only serve as guide for the eye.

(99%, Sigma-Aldrich) were thoroughly mixed for the synthesis of $La_{1.3}Sr_{1.7}Mn_2O_7$. The powder was calcined at 800 °C for 12 h in air. After calcination, the powder was reground, pelletized, and sintered three times at 1350 °C in air with a dwell time of 24 h. Before each sintering, the sample was reground and pelletized again.

Iodometric titration was used to determine the average oxidation state of Mn in $La_{1.3}Sr_{1.7}Mn_2O_7$. 50 mg of the sample was dissolved in 1 M HCL containing an excess of KI. Starch solution was added as an indicator and the titration was performed using a standardized $Na_2S_2O_3$ solution (concentration of 0.01 mol L^{-1}). Three independent measurements were performed to determine the average oxidation state.

X-ray powder diffraction measurements were done on a Bruker D8 Advance diffractometer in Bragg–Brentano geometry with CuKα radiation (VANTEC detector). For the electrochemical cells, a measurement range of 5–80° (2θ) was used, with a step size of 0.006°. To prevent possible side reactions with air, all the samples were loaded into an air-tight low background specimen holder (Bruker A100B36/B37) and sealed inside an argon-filled glovebox before the measurements. Rietveld refinement was done using TOPAS V6. A reference scan of LaB$_6$ (NIST 660a) was used as a basis for empirical determination of the instrumental intensity distribution.

The electrochemical cell preparations were done in an argon-filled glove box to prevent any contact with air. The electrolyte material $La_{0.9}Ba_{0.1}F_{2.9}$ was prepared by ball milling stoichiometric amounts of LaF$_3$ (99.9%, STREM Chemicals) and BaF$_2$ (99%, STREM chemicals) for 12 h at 600 rpm (based on ref. [40]). The cathode composite was prepared with a weight ratio of 30:60:10 with regard to $La_{1.3}Sr_{1.7}Mn_2O_7$, the electrolyte and carbon black, respectively. The mixture was ball milled for 1 h at 250 rpm. For the preparation of the anode composite, elemental Pb (≥99%, Sigma-Aldrich), PbF$_2$ (99+%, STREM Chemicals), and carbon black were ball milled in a weight ratio of 45:45:10 for 12 h at 600 rpm.

Cells were prepared by pressing together 200 mg of electrolyte, 7 mg of cathode composite and 8.5 mg of anode composite at a pressure of 2 tons. The dimensions of the resulting pellets were measured to be approximately 1.3 mm in thickness and 7.3 mm in diameter. The pellets were spring-loaded in a modified Swagelok-type cell.

For the galvanostatic charge/discharge measurements, the cells were heated to 170 °C. A potentiostat (either Biologic SP-150 or Solartron Analytical 1400 CellTest System) was used for the charge–discharge cycling. The charging currents were chosen such that the respective cathode material was charged with a C/20 rate. In case of 0.0021 g of the active material of $La_{1.3}Sr_{1.7}Mn_2O_7$, this corresponds to a charging current of 5.1 µA.

Magnetic measurements were done using a Quantum Design MPMS SQUID magnetometer. The cathode composite was scratched off the cells and filled into a gelatin capsule and fixed into a plastic sample holding straw. $M(T)$ curves were measured in a field cooled (FC) mode from 300 K to 10 K at 1 T field. $M(H)$ measurements were done at 10 K between −5 and 5 T.

Supporting Information

Supporting Information is available from the Wiley Online Library or from the author.

Acknowledgements

1900974 (8 of 9)

Conflict of Interest

The authors declare no conflict of interest.

Keywords

[1] A. Molinari, H. Hahn, R. Kruk, *Adv. Mater.* **2019**, *31*, 1806662.

[2] C. Navarro-Senent, A. Quintana, E. Menendez, E. Pellicer, J. Sort, *APL Mater.* **2019**, *7*, 030701.

[3] F. Zavaliche, H. Zheng, L. Mohaddes-Ardabili, S. Y. Yang, Q. Zhan, P. Shafer, E. Reilly, R. Chopdekar, Y. Jia, P. Wright, D. G. Schlom, Y. Suzuki, R. Ramesh, *Nano Lett.* **2005**, *5*, 1793.

[4] S. Ghosh, C. Lemier, J. Weissmuller, *IEEE Trans. Magn.* **2006**, *42*, 3617.

[5] R. O. Cherifi, V. Ivanovskaya, L. C. Phillips, A. Zobelli, I. C. Infante, E. Jacquet, V. Garcia, S. Fusil, P. R. Briddon, N. Guiblin, A. Mougin, A. A. Unal, F. Kronast, S. Valencia, B. Dkhil, A. Barthelemy, M. Bibes, *Nat. Mater.* **2014**, *13*, 345.

[6] M. Liu, Z. Y. Zhou, T. X. Nan, B. M. Howe, G. J. Brown, N. X. Sun, *Adv. Mater.* **2013**, *25*, 1435.

[7] J. Lou, M. Liu, D. Reed, Y. H. Ren, N. X. Sun, *Adv. Mater.* **2009**, *21*, 4711.

[8] W. Eerenstein, M. Wiora, J. L. Prieto, J. F. Scott, N. D. Mathur, *Nat. Mater.* **2007**, *6*, 348.

[9] H. J. A. Molegraaf, J. Hoffman, C. A. F. Vaz, S. Gariglio, D. van der Marel, C. H. Ahn, J. M. Triscone, *Adv. Mater.* **2009**, *21*, 3470.

[10] C. A. F. Vaz, J. Hoffman, Y. Segal, J. W. Reiner, R. D. Grober, Z. Zhang, C. H. Ahn, F. J. Walker, *Phys. Rev. Lett.* **2010**, *104*, 127202.

[11] A. K. Mishra, A. J. Darbandi, P. M. Leufke, R. Kruk, H. Hahn, *J. Appl. Phys.* **2013**, *113*.

[12] A. Molinari, H. Hahn, R. Kruk, *Adv. Mater.* **2018**, *30*, 1703908.

[13] M. Weisheit, S. Fahler, A. Marty, Y. Souche, C. Poinsignon, D. Givord, *Science* **2007**, *315*, 349.

[14] A. Quintana, J. Zhang, E. Isarain-Chavez, E. Menendez, R. Cuadrado, R. Robles, M. D. Baro, M. Guerrero, S. Pane, B. J. Nelson, C. M. Muller, P. Ordejon, J. Nogues, E. Pellicer, J. Sort, *Adv. Funct. Mater.* **2017**, *27*, 1701904.

[15] Q. Zhang, X. Luo, L. Wang, L. Zhang, B. Khalid, J. Gong, H. Wu, *Nano Lett.* **2016**, *16*, 583.

[16] S. Dasgupta, B. Das, Q. Li, D. Wang, T. T. Baby, S. Indris, M. Knapp, H. Ehrenberg, K. Fink, R. Kruk, H. Hahn, *Adv. Funct. Mater.* **2016**, *26*, 7507.

[17] G. Wei, L. Wei, D. Wang, Y. Chen, Y. Tian, S. Yan, L. Mei, J. Jiao, *Sci. Rep.* **2017**, *7*, 12554.

[18] T. Yamada, K. Morita, K. Kume, H. Yoshikawa, K. Awaga, *J. Mater. Chem. C* **2014**, *2*, 5183.

[19] S. Dasgupta, B. Das, M. Knapp, R. A. Brand, H. Ehrenberg, R. Kruk, H. Hahn, *Adv. Mater.* **2014**, *26*, 4639.

[20] K. Duschek, A. Petr, J. Zehner, K. Nielsch, K. Leistner, *J. Mater. Chem. C* **2018**, *6*, 8411.

[21] A. Quintana, E. Menendez, M. O. Liedke, M. Butterling, A. Wagner, V. Sireus, P. Torruella, S. Estrade, F. Peiro, J. Dendooven, C. Detavernier, P. D. Murray, D. A. Gilbert, K. Liu, E. Pellicer, J. Nogues, J. Sort, *ACS Nano* **2018**, *12*, 10291.

[22] M. Gossler, M. Albu, G. Klinser, E. M. Steyskal, H. Krenn, R. Wurschum, *Small* **2019**, *15*, 1904523.

[23] M. A. Reddy, M. Fichtner, *J. Mater. Chem.* **2011**, *21*, 17059.

[24] C. Rongeat, M. A. Reddy, R. Witter, M. Fichtner, *ACS Appl. Mater. Interfaces* **2014**, *6*, 2103.

[25] M. A. Reddy, M. Fichtner, in *Handbook of Solid State Batteries* (Ed: N. J. Dudne), Vol. *6*, World Scientific, Singapore **2015**, p. 277.

[26] O. Clemens, C. Rongeat, M. A. Reddy, A. Giehr, M. Fichtner, H. Hahn, *Dalton Trans.* **2014**, *43*, 15771.

[27] M. A. Nowroozi, K. Wissel, J. Rohrer, A. R. Munnangi, O. Clemens, *Chem. Mater.* **2017**, *29*, 3441.

[28] M. A. Nowroozi, O. Clemens, *ACS Appl. Energy Mater.* **2018**, *1*, 6626.

[29] M. A. Nowroozi, S. Ivlev, J. Rohrer, O. Clemens, *J. Mater. Chem. A* **2018**, *6*, 4658.

[30] K. Wissel, S. Dasgupta, A. Benes, R. Schoch, M. Bauer, R. Witte, A. D. Fortes, E. Erdem, J. Rohrer, O. Clemens, *J. Mater. Chem. A* **2018**, *6*, 22013.

[31] L. D. Aikens, L. J. Gillie, R. K. Li, C. Greaves, *J. Mater. Chem.* **2002**, *12*, 264.

[32] C. Greaves, J. L. Kissick, M. G. Francesconi, L. D. Aikens, L. J. Gillie, *J. Mater. Chem.* **1999**, *9*, 111.

[33] M. Kubota, H. Fujioka, K. Ohoyama, K. Hirota, Y. Moritomo, H. Yoshizawa, J. Endoh, *J. Phys. Chem. Solids* **1999**, *60*, 1161.

[34] M. Kubota, H. Fujioka, K. Hirota, K. Ohoyama, Y. Moritomo, H. Yoshizawa, Y. Endoh, *J. Phys. Soc. Jpn.* **2000**, *69*, 1606.

[35] M. A. Nowroozi, K. Wissel, S. Plana-Ruiz, U. Kolb, M. Donzelli, N. Hosseinpourkahvaz, S. Ivlev, F. Kraus, O. Clemens, unpublished.

[36] A. Wang, S. Kadam, H. Li, S. Shi, Y. Qi, *npj Comput. Mater.* **2018**, *4*.

[37] M. Al-Mamouri, P. P. Edwards, C. Greaves, M. Slaski, *Nature* **1994**, *369*, 382.

[38] I. Mohammad, R. Witter, M. Fichtner, A. Reddy, *ACS Appl. Energy Mater.* **2018**, *1*, 4766.

[39] V. K. Davis, C. M. Bates, K. Omichi, B. M. Savoie, N. Momčilović, Q. Xu, W. J. Wolf, M. A. Webb, K. J. Billings, N. H. Chou, S. Alayoglu, R. K. McKenney, I. M. Darolles, N. G. Nair, A. Hightower, D. Rosenberg, M. Ahmed, C. J. Brooks, T. F. Miller III, R. H. Grubbs, S. C. Jones, *Science* **2018**, *362*, 1144.

[40] C. Rongeat, M. A. Reddy, R. Witter, M. Fichtner, *ACS Appl. Mater. Interfaces* **2014**, *6*, 2103.